RESEARCH ARTICLE SUMMARY

SOLAR CELLS

Gas chromatography–mass spectrometry analyses of encapsulated stable perovskite solar cells

Lei Shi*, Martin P. Bucknall, Trevor L. Young, Meng Zhang, Long Hu, Jueming Bing, Da Seul Lee, Jincheol Kim, Tom Wu, Noboru Takamure, David R. McKenzie, Shujuan Huang, Martin A. Green, Anita W. Y. Ho-Baillie*

INTRODUCTION: Although advances in materials and processing have led to remarkable advancements in the energy conversion efficiency of perovskite solar cells (PSCs), increasing from 3.8% to 25.2% in only 10 years, these solar cells cannot become commercially viable unless their underperforming durability is improved. The instability of perovskites must be addressed if PSCs are to compete with silicon technology, which currently offers a 25-year performance warranty. Previous approaches to this problem include the use of metal oxide barrier layers and butyl rubber sealants. Here, we report a low-cost polymer/glass stack encapsulation scheme that enables PSCs to pass the demanding International Electrotechnical Commission (IEC) 61215:2016 Damp Heat and Humidity Freeze tests. These tests help to determine whether solar cell modules can withstand the effects of outdoor operating conditions by exposing them to repeated temperature cycling (–40° to 85°C) as well as 85% relative humidity. Our airtight encapsulation scheme prevented moisture ingress. It was also effective in suppressing outgassing of decomposition products, which limits decomposition reactions of organic hybrid PSCs by allowing these reactions to come to equilibrium. The gas compositions were verified by gas chromatography–mass spectrometry (GC-MS).

RATIONALE: In the GC-MS technique, gas chromatography separates the components in a mixture, and the chemical identity of each component is determined with mass spectrometry. We could directly identify with high specificity the decomposition products of multi-cation perovskite precursors, of unencapsulated perovskite test structures, and of encapsulated full cells at elevated temperatures. The results allowed us to identify thermal degradation pathways by determining the outgassing products of mixed-cation perovskites during heating. We then used GC-MS to evaluate the effectiveness of different packaging techniques developed for PSCs. The packaging schemes were a polyisobutylene (PIB)–based polymer blanket encapsulation, a polyolefin-based blanket encapsulation, and a PIB edge seal. These packaging layers were then capped by a glass cover. For the edge seal, the decomposition gases inside the cell were sampled with a syringe. The feasibilities of these packaging techniques were also demonstrated by IEC photovoltaic module standard Damp Heat and Humidity Freeze testing.

RESULTS: Signature decomposition products such as CH_3I, CH_3Br, and NH_3 were identified and decomposition pathways were proposed for CH_3NH_3I (MAI), $HC(NH_2)_2I$ (FAI), CH_3NH_3Br (MABr), and mixed-cation and mixed-halide $(FAI)_{0.85} + (MABr)_{0.15}$ perovskite precursors, including their secondary decomposition reactions at 350°, 140°, and 85°C. The GC-MS results confirmed that the Br-containing precursor was less prone to thermal decomposition than an I-containing precursor. Also, CsFAMA cells were found to outgas one-fifth as much decomposition product as their FAMA counterparts, which indicated that the Cs-containing cells had better thermal stability. Although the decomposition of FAI is reversible, the mixing of MA with FA precursors caused decomposition products to participate in the secondary reaction that was irreversible. This finding confirmed the disadvantage of mixing of MA with FA perovskite through the reduction in chemical stability. The blanket-encapsulated PSCs sustained no efficiency degradation after 1800 hours of Damp Heat testing or 75 cycles of Humidity Freeze testing.

CONCLUSION: GC-MS identified signature volatile products of the decomposition of organic hybrid perovskites under thermal stress, thereby informing decomposition pathways. The findings are important for developing potential cell-stabilizing strategies, given that cells in the field typically experience high operating temperatures. In addition, results of GC-MS confirm that the low-cost pressure-tight encapsulation we developed is effective in suppressing such outgassing and therefore decomposition reactions of PSCs. This encapsulation scheme is the simplest of all for perovskite cells to pass IEC photovoltaic module standard tests. Our approach can be applied to evaluating the effectiveness of other packaging approaches, as well as testing the effectiveness of coatings and material compositions aimed at limiting light and thermal degradation. ■

ON OUR WEBSITE

Read the full article at https://dx.doi.org/10.1126/science.aba2412

The list of author affiliations is available in the full article online.
*Corresponding author. Email: anita.ho-baillie@sydney.edu.au (A.W.Y.H.-B.); lei.shi@unsw.edu.au (L.S.)
Cite this article as L. Shi *et al.*, *Science* **368**, eaba2412 (2020). DOI: 10.1126/science.aba2412

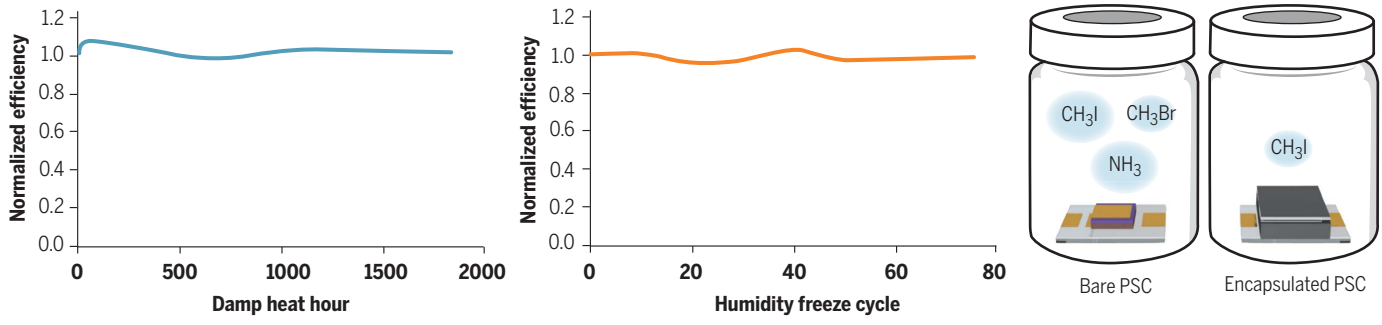

Stable perovskite solar cells exceeding the requirements of the IEC 61215 Damp Heat and Humidity Freeze tests. Unencapsulated and encapsulated perovskite cells were analyzed by gas chromatography–mass spectrometry, detecting signature volatile products of the organic hybrid perovskite decomposition under thermal stress and confirming the effectiveness of the low-cost pressure-tight polymer/glass stack encapsulation schemes developed.

RESEARCH ARTICLE

SOLAR CELLS

Gas chromatography–mass spectrometry analyses of encapsulated stable perovskite solar cells

Lei Shi[1]*, Martin P. Bucknall[2,3], Trevor L. Young[1], Meng Zhang[1,4], Long Hu[5], Jueming Bing[1,6,7], Da Seul Lee[1], Jincheol Kim[1,8], Tom Wu[5], Noboru Takamure[6], David R. McKenzie[6], Shujuan Huang[1,9], Martin A. Green[1], Anita W. Y. Ho-Baillie[1,6,7]*

Although perovskite solar cells have produced remarkable energy conversion efficiencies, they cannot become commercially viable without improvements in durability. We used gas chromatography–mass spectrometry (GC-MS) to reveal signature volatile products of the decomposition of organic hybrid perovskites under thermal stress. In addition, we were able to use GC-MS to confirm that a low-cost polymer/glass stack encapsulation is effective in suppressing such outgassing. Using such an encapsulation scheme, we produced multi-cation, multi-halide perovskite solar cells containing methylammonium that exceed the requirements of the International Electrotechnical Commission 61215:2016 standard by surviving more than 1800 hours of the Damp Heat test and 75 cycles of the Humidity Freeze test.

Metal halide perovskite solar cells (PSCs) have undergone substantial improvements in power conversion efficiency (PCE), which has increased from 3.8% to 25.2% in only 10 years (*1*–*4*). Coupled with its potential for low fabrication cost (*5*), PSC technology is very promising either as a stand-alone perovskite cell or as a top cell in a tandem device. For PSCs to be commercially viable, however, they need to endure long-term environmental stresses imposed by moisture (*6*–*12*), heat (*12*–*17*), and light (*17*–*19*). Over the years, industry and research groups have developed technologies for moisture barriers (*20*–*24*) such as epoxy, butyl rubber, ceramic thin films, and dyads, which can effectively isolate perovskite and organic solar cells from high-humidity environments (*25*–*29*). Other strategies of varying cell design and material choice to improve moisture and thermal stability include altering three-dimensional (3D) perovskite composition (*30*–*34*), applying 2D perovskite material (*35*–*39*), and using alternative electron/hole transport materials (*7*, *40*–*43*). Light stability is also effectively improved by some of these methods (*34*, *42*, *44*–*47*).

One strategy to improve the thermal stability of PSCs is to suppress stress-induced gaseous decomposition of the perovskite materials, which can be achieved by a pressure-tight coverage or encapsulation using materials such as Al_2O_3, aluminum zinc oxide, and SnO_2 (*48*–*52*). Lee *et al.* deposited four layers of organic/inorganic dyads (thickness >1 μm) by initiated chemical vapor deposition and atomic layer deposition (ALD) onto $(FAPbI_3)_{0.87}(MAPbBr_3)_{0.13}$ PSCs [FA = formamidinium; MA = methylammonium (CH_3NH_3)], which maintained 95% of their initial efficiency after 300 hours of storage in the dark at 50°C and 50% relative humidity (RH) (*50*). Bush *et al.* used an ALD SnO_2/zinc tin oxide bilayer and a sputtered indium tin oxide (ITO) layer as the barrier and contact layer, respectively; a $Cs_{0.17}FA_{0.83}Pb(I_{0.83}Br_{0.17})_3$ cell, when encapsulated by glass/ethylene vinyl acetate (EVA)/glass and edge-sealed by butyl rubber, endured 1000 hours at 85°C and 85% RH (*46*). This was the first PSC reported to pass the International Electrotechnical Commission (IEC) 61215:2016 Damp Heat test. In their work, cesium-formamidinium (Cs-FA) was used as the mixed cation because of its thermal stability (*32*). However, a mixed-cation PSC able to pass this test would be more desirable if it contained MA because it offers higher flexibility for composition engineering and because MA-containing mixed-cation PSCs have higher performance potential (*53*). Boyd *et al.* managed to stabilize $MAPbI_3$ PSCs by using a similar SnO_2/ITO barrier layer where ITO not only covers the PSC but "wraps around" the cell, such that the barrier stack covers the perovskite edges to inhibit the escape of volatile species from decomposed $MAPbI_3$ perovskite. As a result, cells were stable at 85°C for 1000 hours in inert atmosphere without any additional encapsulation (*49*). These barrier layers, however, require vacuum processes and their deposition conditions must be tuned such that they do not affect the performance of the PSC; such factors inevitably increase the fabrication cost.

In terms of characterizing heat-induced mass loss from $MAPbI_3$, thermal gravimetric analysis (TGA) has shown that $MAPbI_3$ reversibly decomposes to methylamine (CH_3NH_2) and hydrogen iodide (HI), leaving PbI_2 as the solid remnant (*54*, *55*). Coupling thermal analysis with Fourier transform infrared spectroscopy (FTIR), Williams *et al.* showed that MAI (CH_3NH_3I) does not release gaseous products until 240°C (*56*). No methylamine (CH_3NH_2) was detected, but CH_3I and NH_3 were found (*56*, *57*). Given that their samples were perovskite precursor solutions, the findings were convoluted with the dimethylformamide (DMF) solvent signals. Juarez-Perez *et al.* used TGA–mass spectrometry (MS) to investigate the mass loss of solvent-free $MAPbI_3$ single crystals and determined that the gaseous products released are a mixture of CH_3NH_2, HI, CH_3I, and NH_3 (*58*). They also (*59*) found that $MAPbI_3$ and $MAPbBr_3$ thin films started thermal decomposition within an hour of annealing in high vacuum (~10^{-6} torr) at typical solar cell operation temperatures (40° to 60°C). However, the possible presence of DMF solvent residue might have interfered with the results, as its mass spectrum overlaps with those of some of the decomposition products. It is challenging for FTIR and MS to unambiguously identify unknown compounds or multiple known compounds in a mixture (e.g., perovskites with encapsulants) that are detected simultaneously. By contrast, for TGA, the mass loss that led to the cell efficiency drop could be well below the detection limit because perovskite decomposition can start at surfaces or interfaces and proceeds in a layer-by-layer manner (*60*). More recently, Juarez-Perez *et al.* used microwave rotational spectroscopy to unambiguously detect CH_3I and CH_3NH_2 from $MAPbI_3$ decomposition at 280°C (*61*), identifying more than one decomposition pathway. However, HI and NH_3 could not be detected by their spectroscopy setup because the lowest transitions for these two species were beyond the upper frequency limit.

Although much of the reported PSC stability research was conducted at 85°C (table S1), photovoltaic modules in real-world outdoor conditions must be able to withstand a combination of moisture ingress and temperature extremes. The IEC 61215:2016 Damp Heat, Thermal Cycling, and Humidity Freeze tests (*62*) (Table 1) are among the standard accelerated tests specified for commercial modules. Such modules must survive these tests with less than

[1]Australian Centre for Advanced Photovoltaics, School of Photovoltaic and Renewable Energy Engineering, University of New South Wales, Sydney, NSW 2052, Australia. [2]Bioanalytical Mass Spectrometry Facility, Mark Wainwright Analytical Centre, University of New South Wales, Sydney, NSW 2052, Australia. [3]School of Optometry and Vision Science, University of New South Wales, Sydney, NSW 2052, Australia. [4]Institute of Photovoltaics, Southwest Petroleum University, Chengdu 610500, China. [5]School of Materials Science and Engineering, University of New South Wales, Sydney, NSW 2052, Australia. [6]School of Physics, University of Sydney, Sydney, NSW 2006, Australia. [7]University of Sydney Nano Institute, University of Sydney, Sydney, NSW 2006, Australia. [8]New and Renewable Energy Research Center, Korea Electronics Technology Institute, Seong-Nam, Republic of Korea. [9]School of Engineering, Macquarie University, Sydney, NSW 2109, Australia.
*Corresponding author. Email: anita.ho-baillie@sydney.edu.au (A.W.Y.H.-B.); lei.shi@unsw.edu.au (L.S.)

Table 1. Specifications of the three IEC 61215:2016 tests.

Test	Conditions	Min. T_{95}
Damp Heat	85°C, 85% RH	1000 hours
Thermal Cycling	−40°C (15 min dwell) to 85°C (15 min dwell) Ramp rate of 100°C/hour	200 cycles
Humidity Freeze	50 rounds of Thermal Cycling as prerequisite, followed by −40°C (30 min dwell) to 85°C, 85% RH (20 hours dwell) Ramp rate of 100°C/hour for 0°C ↔ 85°C Ramp rate of 200°C/hour for 0°C ↔ −40°C	10 cycles

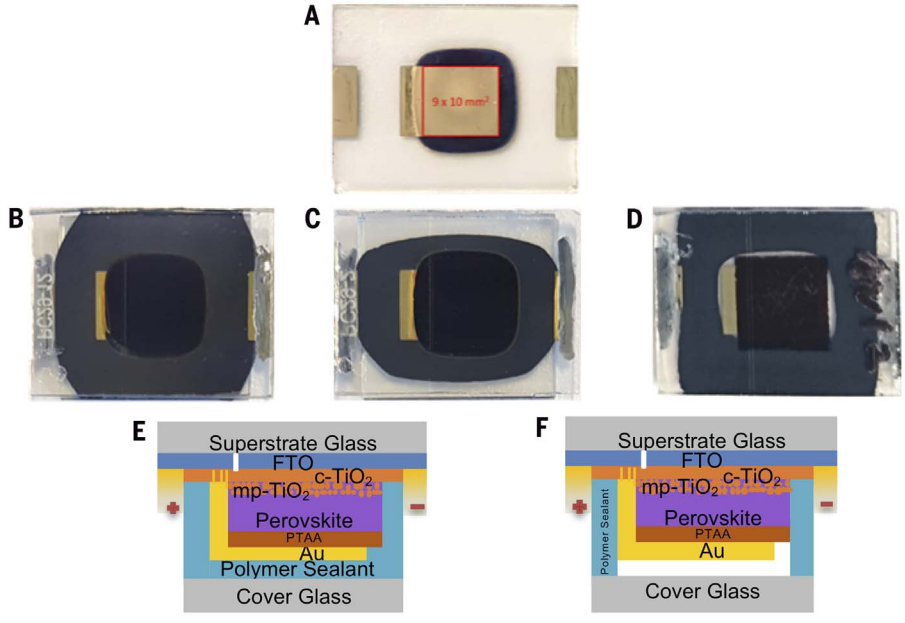

Fig. 1. Solar cells for IEC 61215:2016 Damp Heat and Thermal Cycling tests. (**A**) "Rear" or metal-side view of PSC before packaging (red square denotes the active area). (**B** to **D**) "Front" view (from the superstrate side) of PSC after PIB-based blanket encapsulation (B), PO-based blanket encapsulation (C), and PIB edge seal (D). (**E** and **F**) Illustrations of the cross sections of the respective encapsulation schemes (not to scale).

5% relative loss in efficiency. The Humidity Freeze test, a combination of Damp Heat and Thermal Cycling, therefore exerts the harshest stress on solar cells and their encapsulation. For example, ingressed moisture inside the encapsulation will solidify during freezing and subsequently delaminate the encapsulant. Temperature cycling can promote the decomposition of perovskites (*58*), which itself can accelerate the decomposition reaction. Therefore, weakness in the encapsulation or instability in the perovskite material, if they exist, will most likely be revealed by the Humidity Freeze test.

Previously, we reported a low-cost and effective polyisobutylene (PIB)–based polymeric "blanket-cover" encapsulation scheme for planar $FAPbI_3$ cells passing the IEC 61215:2016 Thermal Cycling test (200 cycles of oscillation between −40° and 85°C) that survived 500 hours in Damp Heat without degradation (*25*). We found that the edge-seal packaging scheme is less effective than the blanket-cover approach and hypothesized that the success of the latter is due to its ability to suppress the outgassing of volatile decomposition products. Here, we developed an improved packaging sequence and applied it to $Cs_{0.05}FA_{0.8}MA_{0.15}Pb(I_{0.85}Br_{0.15})_3$ and $FA_{0.85}MA_{0.15}Pb(I_{0.85}Br_{0.15})_3$. The resulting MA-containing perovskite cells were able to pass the IEC6 1215:2016 Damp Heat and Humidity Freeze tests.

Additionally, we used gas chromatography–mass spectrometry (GC-MS) to directly identify with high specificity the decomposition products of perovskite precursors, unencapsulated and encapsulated perovskite test structures, and full cells at elevated temperature. The findings confirm the outgassing behavior of multication mixed halide perovskites and identify thermal degradation pathways. We then used GC-MS to quantitatively confirm the effectiveness of the polymer blanket cover in conjunction with glass in suppressing such outgassing. This encapsulation scheme demonstrates the feasibility of developing a simple, low-cost packaging technique for stable perovskite cells.

PIB encapsulated and edge-sealed cells

The solar cell structure used was FTO/c-TiO_2/mp-TiO_2/perovskite/PTAA/Au (FTO = fluorine-doped tin oxide; c-TiO_2 = compact TiO_2; mp-TiO_2 = mesoporous TiO_2; PTAA = poly[bis(4-phenyl)(2,4,6-trimethylphenyl)amine]) (Fig. 1, E and F). The composition of the perovskite layer was either $Cs_{0.05}FA_{0.8}MA_{0.15}Pb(I_{0.85}Br_{0.15})_3$ (i.e., CsFAMA) or $FA_{0.85}MA_{0.15}Pb(I_{0.85}Br_{0.15})_3$ (i.e., FAMA).

Figure 1A shows the view from the "rear" or Au side of cell before packaging; Fig. 1, B to D, shows the "front" of the cell (viewing from the superstrate side) after PIB-based polymer (PVS 101) blanket encapsulation, polyolefin (PO)–based polymer blanket encapsulation, and PIB edge seal, respectively. Figure 1, E and F, illustrates the cross sections of the respective encapsulation schemes. Note that the PO used in this work is slightly narrower than the PIB used. The effect of the width of the polymer tape on cell durability is discussed below.

PCE was maintained after encapsulation (table S4). The packaged devices were then subjected to the IEC Damp Heat and Humidity Freeze tests (as specified in Table 1) in an environmental chamber (fig. S2B). The cells' PCEs were measured ex situ at regular intervals. Results are plotted in Fig. 2 and summarized in Table 2.

Regarding cells that underwent the Damp Heat test, PIB-based blanket-encapsulated cells sustained no degradation after 1800 hours, far exceeding the requirement specified by the IEC 61215:2016 standard (1000 hours). The short-circuit current density (J_{SC}) and open circuit voltage (V_{OC}) remained reasonably stable throughout the test, whereas the fill factor (FF) increased by more than 10% relative (fig. S3, A to C). Negligible change in the x-ray diffraction pattern of the CsFAMA perovskite film was observed after 1800 hours of Damp Heat (fig. S3D). On the other hand, PCEs of PIB edge-sealed cells degraded by 30% in the first 200 hours, which is consistent with the observations of edge-sealed $FAPbI_3$ devices in our previous work (*25*). We believe that such a degradation is due to heat-induced decomposition rather than moisture ingress (see below).

Regarding cells that underwent the Humidity Freeze test, PIB-based blanket-encapsulated cells also passed the IEC 61215:2016 test; in particular, the CsFAMA cells experienced no

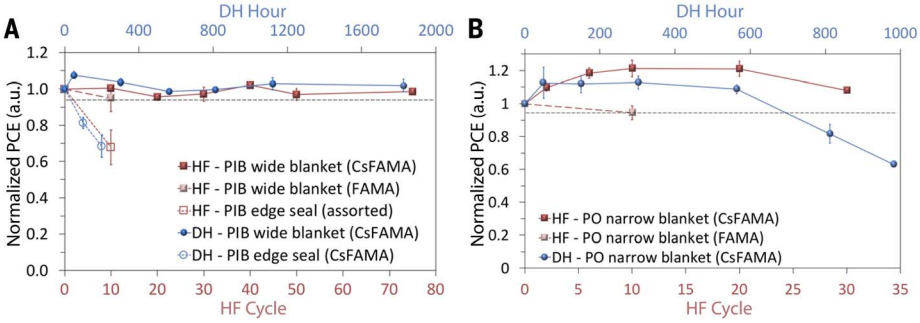

Fig. 2. Results of the IEC 61215:2016 tests demonstrating the effectiveness of packaging schemes. (**A** and **B**) PCE evolution of PIB-encapsulated or edge-sealed PSCs (A) and PO-encapsulated PSCs (B) during Damp Heat (DH) and Humidity Freeze (HF) tests. The dashed lines denote 5% relative PCE loss, which is the maximum allowed by the IEC standard after 1000 hours of Damp Heat or 10 cycles of Humidity Freeze. Error bars denote SD. See Table 2 for absorber composition, quantity, and result summary.

Table 2. Summary of results of Damp Heat and Thermal Cycling tests for PSCs edge-sealed or encapsulated using three different methods.

Test	Encapsulation	No. of samples	Perovskite	T_{95}	Result
Damp Heat	PIB wide blanket	3	CsFAMA	>1800 hours	Pass
	PO narrow blanket	3	CsFAMA	>564 hours	Fail
	PIB edge seal	4	CsFAMA	<100 hours	Fail
Humidity Freeze	PIB wide blanket	4	CsFAMA	>75 cycles	Pass
	PIB wide blanket	2	FAMA	10 cycles	Pass
	PO narrow blanket	4	CsFAMA	>30 cycles	Pass
	PO narrow blanket	3	FAMA	10 cycles	Pass
	PIB edge seal	4	CsFAMA × 2, FAMA × 2	<<10 cycles	Fail

degradation after 75 Humidity Freeze cycles, which is 7.5 times the number required by the IEC 61215:2016 standard. Their J_{SC}, V_{OC}, and FF values were also stable throughout the test (fig. S3, A to C). Interestingly, FAMA cells also passed the 10 cycles required for such tests (taking into account the 50 prerequisite rounds of Thermal Cycling), with average PCE dropping by only 5% after the test. Similar to the Damp Heat test result, PIB edge-sealed PSCs failed the Humidity Freeze test, suffering 30% PCE degradation after 10 Humidity Freeze cycles.

PO encapsulated cells

As edge sealing is the less ideal packaging method, only the blanket approach was tested for PO-encapsulated PSCs. However, the width of the PO tape available from the supplier is narrower than that of the PIB tape. Although the PCEs of PO-encapsulated PSCs increased initially during the Damp Heat test, they decreased after 600 hours. Both J_{SC} and FF contributed to PCE loss (fig. S4, A and C). The decomposition of the perovskite layer induced by the gradual moisture ingress can be seen in fig. S5A; the absorber layer area diminishes from the edges toward the center, revealing the underlying gold after 800 hours of Humidity Freeze. This is due to the smaller size of the available PO tape that covered only 2 mm of edge margin at the narrowest part, resulting in weaker performance than for the wider PIB tape, which covered the entire edge margin (5 to 6 mm). Wider PO coverage may allow PSCs to sustain the 1000 hours required for the Damp Heat test. The slight increase in V_{OC} (fig. S4B) is due to the slight bandgap increase of the perovskite evidenced by the slight blue shift of the photoluminescence peak (fig. S5B), owing to the possible halide segregation induced by heat and moisture ingress.

PO-encapsulated CsFAMA cells sustained no degradation after 30 cycles of the Humidity Freeze test, again exceeding the IEC 61215:2016 standard. In addition, their PCEs increased by 10 to 20% relative. No moisture ingress was visible in these PSCs after 30 cycles of Humidity Freeze. Figure S4 shows that the J_{SC} and V_{OC} of the cells remained stable and that FF improved by more than 20% relative, which contributed to the observed PCE increase. Without Cs in the perovskite, FAMA cells survived only 10 Humidity Freeze cycles with an average PCE drop of 5%, although they still met the IEC 61215:2016 requirement. The better stability provided by Cs has been verified by GC-MS (see below). Nonetheless, we can conclude that the PO encapsulant is robust in terms of its ability to withstand extreme thermal cycles.

Overall, the excellent stability of the encapsulated PSCs reported here is attributed to the pressure-tight environment provided by the polymer/glass packaging, which effectively suppressed outgassing and thermal decomposition of the PSCs during the accelerated lifetime testing. Both hypotheses are verified by the following GC-MS experiments.

Gas chromatography–mass spectrometry analysis

Automated headspace GC-MS analyses (fig. S6) were carried out on three types of samples in this work: organic perovskite precursor powders, unencapsulated test structures, and encapsulated test cells.

Organic perovskite precursor powders

The organic perovskite precursors MAI, FAI, MABr, and $(FAI)_{0.85}$ + $(MABr)_{0.15}$ in powder form were analyzed with the aim of identifying their major decomposition products. This is because organic components of the perovskites have been reported to be the source of volatile products (*17*, *57*–*59*, *63*, *64*). They were sealed in vials and subsequently annealed on a hotplate at three different conditions: 350°C for 15 min, 140°C for 10 hours, and 85°C for 100 hours (*58*, *64*).

Figure 3 summarizes the peak areas of the chromatograms for the annealed precursor materials. After annealing, CH_3I, HCN, and CH_3Br were found to be the major decomposition products from CH_3NH_3I (MAI), $HC(NH_2)_2I$ (FAI), and CH_3NH_3Br (MABr), respectively (Fig. 3A), as evidenced by the chromatograms obtained and shown in fig. S7, A to C, referencing the mass spectra in fig. S8, A to C. In addition, NH_3 was detected in all precursor materials tested (Fig. 3 and fig. S7E). These findings are in agreement with reports of the same decomposition products in the literature (*57*, *59*, *64*). Decomposition reactions of MAI, FAI, and MABr are shown in Eqs. 1 to 3, respectively, according to results from GC-MS. Other reactions, as shown in Eqs. 4a and 4b, have also been reported to be the decomposition pathways (although reversible) for MAI and MABr, respectively (*61*, *63*). However, our results suggest that the CH_3NH_2 is merely an intermediate product of MA decomposition, as the detected amount was negligible (figs. S7F and S8D) relative to other major decomposition products.

$$CH_3NH_3I(s) \xrightarrow{\Delta} CH_3I(g) + NH_3(g) \quad (1)$$

$$HC(NH_2)_2I(s) \xleftrightarrow{\Delta} HCN(g) + NH_3(g) + HI(g) \quad (2)$$

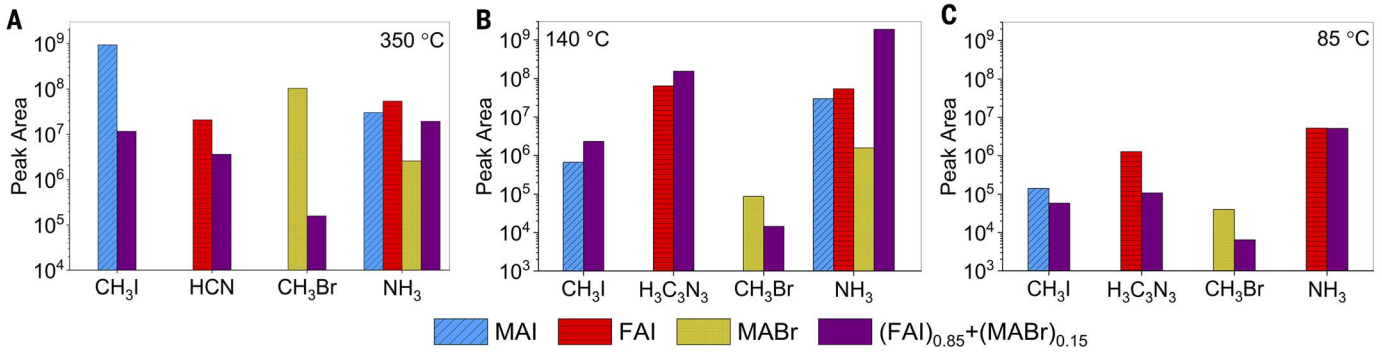

Fig. 3. Signature decomposition products of dry perovskite precursor powders. (**A** to **C**) GC-MS peaks of products after annealing at (A) 350°C for 15 min, (B) 140°C for 10 hours, and (C) 85°C for 100 hours.

$$CH_3NH_3Br(s) \xrightarrow{\Delta} CH_3Br(g)+NH_3(g) \quad (3)$$

$$CH_3NH_3I(s) \xleftrightarrow{\Delta} CH_3NH_2(g)+HI(g) \quad (4a)$$

$$CH_3NH_3Br(s) \xleftrightarrow{\Delta} CH_3NH_2(g)+HBr(g) \quad (4b)$$

For the perovskite precursor FAI annealed at lower temperatures (140°C and 85°C), $H_3C_3N_3$ instead of HCN was found to be the major decomposition product (Fig. 3, B and C, and figs. S9 and S10). Regarding high-temperature (350°C) annealing of the precursor $(FAI)_{0.85}$ + $(MABr)_{0.15}$, the decomposed products of HCN, CH_3Br, and NH_3 detected (Fig. 3A) were expected from the FAI and MABr mixture in 85:15 molar ratio (fig. S7D). However, we also detected CH_3I (Fig. 3A), which is typically a product of MAI decomposition. This could come from the decomposition of a solid solution of $FA_{0.85}MA_{0.15}I_{0.85}Br_{0.15}$ formed by annealing $(FAI)_{0.85}$ + $(MABr)_{0.15}$ at high temperatures (see photos in fig. S11A). This appears to be the case for the 140°C-annealed precursor mixture (fig. S11B) as well, which may be eutectic, given that the melting points of FAI and MABr powders are 242°C and 296°C, respectively.

CH_3I was still detected from $(FAI)_{0.85}$ + $(MABr)_{0.15}$ annealed at the much lower temperature of 85°C (Fig. 3C), despite the lack of solid $FA_{0.85}MA_{0.15}I_{0.85}Br_{0.15}$ solution formed (fig. S11C). Apparently, this CH_3I was mostly produced by the reaction between the CH_3NH_2 and HI as described by Eq. 5 (*63*), where CH_3NH_2 comes from MABr (*65*) (Eq. 4b) and HI comes from FAI (Eq. 2):

$$CH_3NH_2(g)[\text{Eq. 4b}] + HI(g)[\text{Eq. 2}] \xrightarrow{\Delta} CH_3I(g)+NH_3(g) \quad (5)$$

CH_3CN (acetonitrile) (figs. S7, D and H, S8E, and S9A) is also a product of the decomposition of 350°C- and 140°C-annealed $(FAI)_{0.85}$ + $(MABr)_{0.15}$ detected by the QPlot method. It is believed that CH_3CN is the product of HCN (from FAI; Eq. 2) reacting with CH_3X (from MA-containing precursors; Eq. 1, 3, or 5) through a secondary reaction (Eq. 6):

$$HCN(g)[\text{Eq. 2}] + CH_3X(g)[\text{Eq. 1, 3, or 5}] \rightarrow CH_3CN(g)+HX(g), X = \text{I or Br} \quad (6)$$

The secondary reactions that consume CH_3NH_2 [Eq. 4, which is kinetically favorable (*63*)] and HCN [Eq. 6, which has a negative Gibbs free energy change (−45.3 kJ/mol at 350°C and −46.9 kJ/mol at 140°C) (*66*, *67*)] explain why the CH_3Br and HCN peaks (purple histograms) from $(FAI)_{0.85}$ + $(MABr)_{0.15}$ annealed at 350°C were disproportionally lower than the CH_3Br peak from pure MABr (yellow histograms) and the HCN peak from pure FAI (red histogram) (Fig. 3A). Another signature FA-related decomposition product is $H_3C_3N_3$ (*sym*-triazine) (Eq. 7):

$$3HC(NH_2)_2I(s) \xrightarrow{\Delta} H_3C_3N_3(g)+3NH_3(g)+3HI(g) \quad (7)$$

In addition to $H_3C_3N_3$, other FA-related decomposition products include $H_4C_3N_4$ and CHO(NH_2) (formamide) detected by the Amine method (figs. S7G, S8, I to K, S9C, and S10A). $H_4C_3N_4$ detected from the 350°C-annealed precursor could be the product of a reaction between $H_3C_3N_3$ and NH_3 at high temperature. $CH(N_2H_3)$ (formamidine), as reported in (*64*), was not directly detected here, but CHO(NH_2), possibly in its oxidized form, was detected, although the source of oxygen is yet to be ascertained.

Another minor product, CH_3(NH)CHO (methylformamide), was detected specifically from $(FAI)_{0.85}$ + $(MABr)_{0.15}$ (figs. S7G, S8L, S9C, and S10C). This could be formed by CHO(NH_2) reacting with CH_3I, with HI also being a product. Alternatively, CH_3(NH)CHO could be formed by CHO(NH_2) reacting with CH_3NH_2, with NH_3 also being a product (*68*). Methylformamide, more so than CH_3CN, is an interaction product of low temperature–annealed MA and FA mixed powders (fig. S10A).

HI could be detected by the Amine method (fig. S9C) and more reliably by the direct MS analysis method from annealed MAI, FAI, and $(FAI)_{0.85}$ + $(MABr)_{0.15}$ (fig. S12), as predicted by Eqs. 2 and 4a. Likewise, HBr could be detected by the direct MS analysis method from annealed MABr (fig. S13), as predicted by Eq. 3.

For 350°C- and 140°C-annealed precursors, the amount of NH_3 produced was similar from all precursors except MABr, which suggests that MABr is less prone to thermal decomposition. This is because Br^- is a stronger conjugated base of hydrogen halide than I^- (*61*) and has a much higher oxidation potential (*69*), thus favoring the CH_3NH_2/HBr decomposition pathway (Eq. 4b) over the detrimental CH_3Br/NH_3 route (Eq. 3).

From low temperature–annealed MAI and MABr, no NH_3 was detected, possibly because of the reaction between CH_3X (X = I or Br) and NH_3 at low temperature producing ammonia salt, as reported in (*61*). The lack of contribution from MABr to mixed $(FAI)_{0.85}$ + $(MABr)_{0.15}$ in terms of NH_3 product explains the almost identical NH_3 peaks from pure FAI and mixed $(FAI)_{0.85}$ + $(MABr)_{0.15}$ (Fig. 3C).

GC-MS experiments were also performed on CsI and $(CsI)_{0.05}$ + $(FAI)_{0.8}$ + $(MABr)_{0.15}$ powders. The chromatograms (fig. S7H) were similar to those of mixed FAMA precursors without Cs, which suggests no outgassing from CsI (fig. S7I).

These findings illustrate that the mixing of MA with FA perovskite reduces stability, producing decomposition products that otherwise would not be predicted in FA-only perovskites. Although the decomposition of FAI as represented by Eq. 2 is reversible (*64*), when FAI is mixed with MA-containing precursors, the decomposition products participate in the secondary reaction (e.g., Eq. 5), which is irreversible (*61*).

Figure 4 shows the types of unencapsulated test structures and encapsulated test cells analyzed in this work, each designated with a label with prefix "Con." For the GC-MS analyses, these samples were sealed in the vials and

annealed at 85°C for 100 hours to encourage outgassing before GC-MS measurements.

Unencapsulated test structures

Figure 5A compares the GC results of 85°C-annealed unencapsulated test structures Con. 1 (FAMA/PTAA), Con. 2 (PTAA), and Con. 3 (FAMA), all of which were fabricated on FTO/c-TiO_2/mp-TiO_2 glass substrate and covered by Au. After 100 hours, no outgassing could be detected from PTAA thin film (Con. 2) by either the Amine method (Fig. 5A, orange curve) or the QPlot method (fig. S14). This is an encouraging demonstration of the good stability of PTAA.

Similar to the results for 85°C-annealed mixed perovskite precursor powders, the signature decomposition products CH_3I (Fig. 5B), CH_3Br (Fig. 5C), and NH_3 (Fig. 5D) could be detected in unencapsulated Con. 1 test cells using single ion monitoring (SIM) mode by either method. $CHO(NH_2)$, $CH_3(NH)CHO$ (fig. S15F), and a small amount of CH_3NH_2 (intermediate decomposition product) were also detected (see fig. S15G). HCN and $H_3C_3N_3$ were not detected; the absence of HCN as a decomposition product of unencapsulated cells annealed at low temperature agrees with results reported by Ma *et al.* (*57*), who observed HCN release only at temperatures above 285°C and 350°C for FAI and $FAPbI_3$, respectively.

More important, CsFAMA cells outgassed one-fifth as much decomposition product (compare the orange and blue histograms for Con. 1 samples in Fig. 5, B to D) as their FAMA counterparts, indicating better thermal stability of Cs-containing cells.

Encapsulated test cells

In encapsulated cells, the intensities of CH_3I (Fig. 5B), CH_3Br (Fig. 5C), and NH_3 (Fig. 5D) decomposition products were reduced. In addition, CH_3NH_2, HI, $CHO(NH_2)$, and $CH_3(NH)CHO$ could not be detected (fig. S15). PO (Con. 1/PO) was more effective than PIB (Con. 1/PIB) in suppressing CH_3I and CH_3Br outgassing, especially for FAMA cells. Although PO in itself was more permeable to NH_3 than PIB (probably due to the better absorption of NH_3 by PIB during the test), the application of cover glass eliminated NH_3 outgassing in any case (Fig. 5D).

For edge-sealed PSCs, a syringe was used to sample the gas within the cavity between the PSC and the cover glass to look for the major decomposition products. This is a nonintrusive way to analyze chemical decomposition processes without having to disassemble the packaged PSC. Relative to unencapsulated cells, the amounts of CH_3Br and CH_3I detected from edge-sealed cells were also reduced (Fig. 5, B and C, and fig. S15, A and B), showing the effectiveness of the edge sealing.

C_3H_6 was detected from encapsulated structures only (fig. S15, A and B); this C_3H_6 is believed to originate from PIB- or PO-based polymer outgassing and is particularly prominent in manually sampled GC (because of direct contact between PIB and the syringe during manual sampling). Most important, C_3H_6 was successfully distinguished from other perovskite-related signals with similar MS patterns, such as CH_3CN, owing to the high specificity of GC-MS.

The application of cover glass on encapsulated cells successfully suppressed CH_3Br and NH_3 outgassing for either CsFAMA or FAMA cells using any type of encapsulation: blanket or edge-sealed CsFAMA using either PIB or PO. It can be concluded that neither PO nor PIB can completely suppress perovskite outgassing without the use of cover glass. Nonetheless, the polymers function effectively as moisture

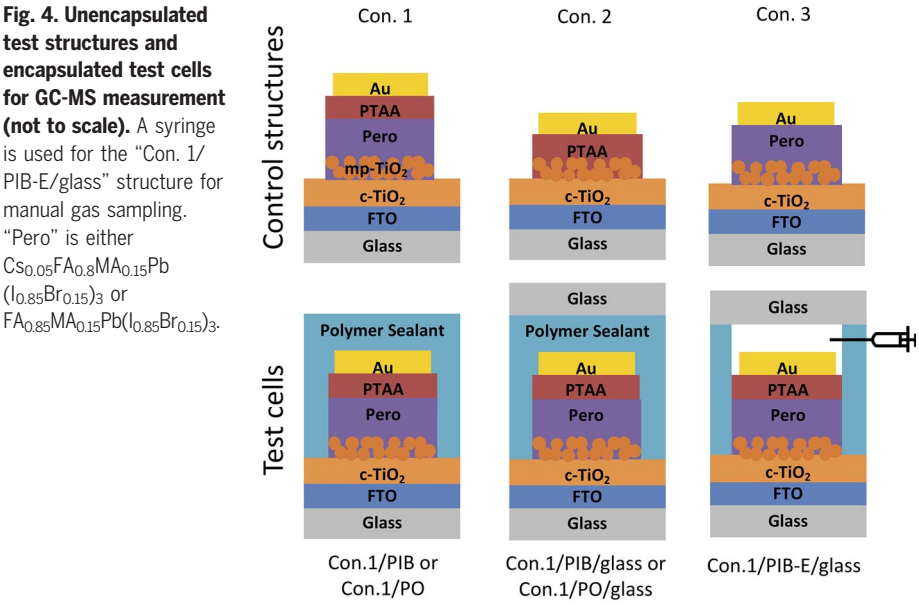

Fig. 4. Unencapsulated test structures and encapsulated test cells for GC-MS measurement (not to scale). A syringe is used for the "Con. 1/PIB-E/glass" structure for manual gas sampling. "Pero" is either $Cs_{0.05}FA_{0.8}MA_{0.15}Pb(I_{0.85}Br_{0.15})_3$ or $FA_{0.85}MA_{0.15}Pb(I_{0.85}Br_{0.15})_3$.

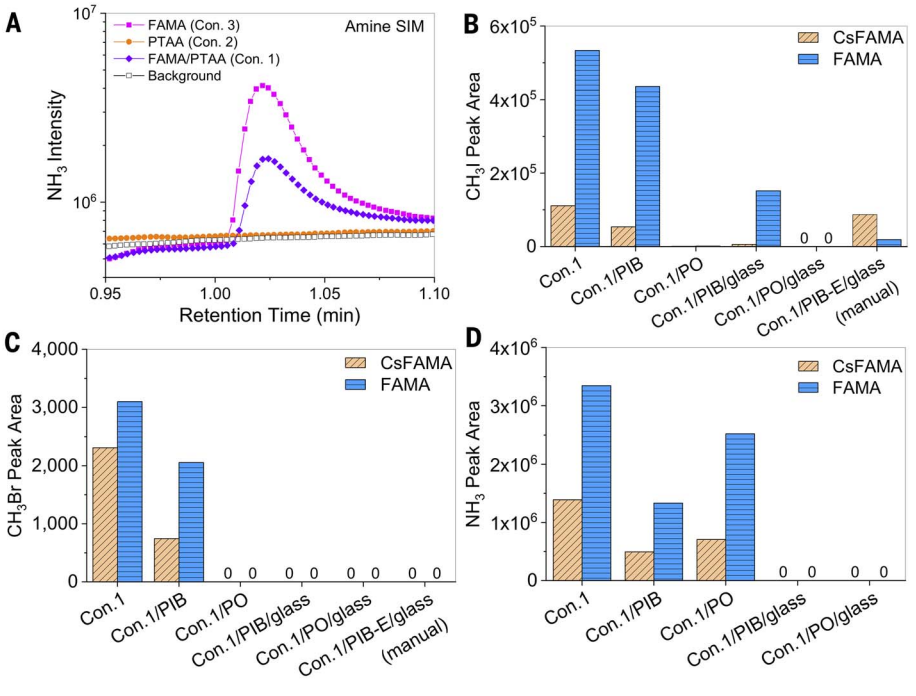

Fig. 5. Signature decomposition products of unencapsulated test structures and encapsulated test cells. (**A**) GC chromatograms for unencapsulated test structures Con. 3 (FAMA), Con. 2 (PTAA), and Con. 1 (FAMA/PTAA) annealed for 100 hours at 85°C. (**B** to **D**) SIM chromatographic peak areas of the signature decomposition products of CH_3I (B), CH_3Br (C), and NH_3 (D) for PSCs with or without packaging, annealed for 100 hours at 85°C.

barriers and as strong adhesives between the PSC and the cover glass. They also have low elastic modulus (0.5 MPa for PIB; 20 MPa for PO) (*70*) and therefore maintain the encapsulation integrity during the harsh conditions simulated by the Humidity Freeze test (*71*).

The polymer/glass blanket encapsulation is an effective scheme providing a pressure-tight environment for the PSC. This causes any decomposition reaction to reach equilibrium quickly before damage occurs to the PSC, as described by Eq. 8. ΔG is the free energy change during the decomposition reaction, $\Delta G°$ is the free energy change when the reactants and products are in their standard states, and Q is the ratio of the product concentration to the reactant concentration. As the concentration of products increases in a pressure-tight environment, Q increases and ΔG tends toward zero, indicating that the reaction reaches equilibrium. The variation of the temperature could even drive ΔG to positive (i.e., unspontaneous) reaction. Sealing the PSC in a pressure-tight environment effectively suppresses the decomposition reaction even when it is not fully reversible, as is the case for MA or FA/MA mixed multi-cation perovskites.

$$\Delta G = \Delta G° + RT \ln Q \qquad (8)$$

Finally, preliminary evaluation of the blanket encapsulation (PIB and PO) scheme by maximum power point tracking (MPPT) with the purpose of evaluating the temperature threshold under constant illumination was carried out on CsFAMA PSCs. The results (fig. S16) show that blanket-encapsulated cells are more stable than edge-sealed cells. Temperatures above 35°C trigger degradations. It is expected that cells with architectures that are less sensitive to ultraviolet light will have better stability.

Conclusion

Our work shows that organic-inorganic PSCs encapsulated with simple and low-cost polyisobutylene- or polyolefin-based polymer-glass combinations have excellent durability exceeding the requirements of the IEC 61215:2016 Damp Heat and Humidity Freeze tests. These results are especially noteworthy because the PSCs used in this study contain MA cations, which are known to have lower thermal stability. Yet these cells survived the Humidity Freeze test, which exerts the harshest humidity and thermal stress. Using GC-MS, we have identified the decomposition products of single, mixed-cation, and mixed-halide perovskite precursor materials as well as completed PSCs with high specificity. On the basis of the identified signature decomposition products such as CH_3I, CH_3Br, and NH_3, we propose decomposition pathways for MAI, FAI, MABr, mixed-cation, and mixed-halide perovskite precursors including their secondary decomposition reactions. We then found that although decomposition pathways are similar for complete PSCs, decomposition is effectively suppressed by the use of polymer–glass blanket encapsulation, which is a hermetic encapsulation scheme creating a pressure-tight environment and preventing the escape of decomposition products. The developments in this work contributes valuable knowledge and advances for stabilizing PSCs, increasing their commercialization prospects.

Methods summary

Details of materials and processes for PSC fabrication, packaging, and characterization can be found in the supplementary materials.

Similar to previous reports, electrical feedthrough was achieved without the use of metal but instead via the FTO layer, ensuring hermeticity (*25*). However, additional edge cleaning steps were applied in this work to ensure good adhesion between the encapsulant and the c-TiO_2 layer.

Automated headspace GC-MS analysis (fig. S6) was performed to investigate the temperature-induced decomposition of PSCs and the effectiveness of different packaging schemes. A sample under analysis was first sealed in a glass vial inside a N_2-filled glovebox before being annealed to generate gaseous substances from the thermal decomposition of the sample inside the vial. After cooling to room temperature, the gas inside the vial was sampled and injected onto the column by the automated headspace GC-MS system. In addition to normal mass-to-charge ratio (m/z) scan mass spectra, SIM was used as a supplementary technique to quantify weaker signals (e.g., for encapsulated cells with very low amounts of CH_3I, HCN, CH_3Br, and NH_3 outgassing). The intensity of each peak was quantified by the peak area using the software. Two columns, a Restek QPLOT column (QPlot method) and a base-deactivated Restek VolatileAmine column (Amine method), were used for GC-MS analysis in this work with different levels of sensitivity. To further improve the specificity of GC-MS results, the identification of key decomposition products was verified by GC-MS measurement of the same standard gas samples (fig. S17, A to D). We used direct MS analysis to detect the highly reactive HI and HBr gases (fig. S17E); these gases could not be reliably detected by GS-MS because of their reaction with the stationary phase of the columns (*72*). More details of the GC-MS methods can be found in the supplementary materials.

REFERENCES AND NOTES

1. M. A. Green, A. Ho-Baillie, H. J. Snaith, The emergence of perovskite solar cells. *Nat. Photonics* **8**, 506–514 (2014). doi: 10.1038/nphoton.2014.134
2. M. A. Green, A. Ho-Baillie, Perovskite Solar Cells: The Birth of a New Era in Photovoltaics. *ACS Energy Lett.* **2**, 822–830 (2017). doi: 10.1021/acsenergylett.7b00137
3. M. A. Green *et al*., Solar cell efficiency tables (version 54). *Prog. Photovolt. Res. Appl.* **28**, 3–15 (2020). doi: 10.1002/pip.3228
4. National Renewable Energy Laboratory, Efficiency Chart (2019); www.nrel.gov/pv/cell-efficiency.html.
5. N. L. Chang *et al*., A manufacturing cost estimation method with uncertainty analysis and its application to perovskite on glass photovoltaic modules. *Prog. Photovolt. Res. Appl.* **25**, 390–405 (2017). doi: 10.1002/pip.2871
6. J. H. Noh, S. H. Im, J. H. Heo, T. N. Mandal, S. I. Seok, Chemical management for colorful, efficient, and stable inorganic-organic hybrid nanostructured solar cells. *Nano Lett.* **13**, 1764–1769 (2013). doi: 10.1021/nl400349b; pmid: 23517331
7. S. N. Habisreutinger *et al*., Carbon nanotube/polymer composites as a highly stable hole collection layer in perovskite solar cells. *Nano Lett.* **14**, 5561–5568 (2014). doi: 10.1021/nl501982b; pmid: 25226226
8. G. Niu *et al*., Study on the stability of $CH_3NH_3PbI_3$ films and the effect of post-modification by aluminum oxide in all-solid-state hybrid solar cells. *J. Mater. Chem. A* **2**, 705–710 (2014). doi: 10.1039/C3TA13606J
9. J. A. Christians, P. A. Miranda Herrera, P. V. Kamat, Transformation of the excited state and photovoltaic efficiency of $CH_3NH_3PbI_3$ perovskite upon controlled exposure to humidified air. *J. Am. Chem. Soc.* **137**, 1530–1538 (2015). doi: 10.1021/ja511132a; pmid: 25590693
10. M. I. Asghar, J. Zhang, H. Wang, P. D. Lund, Device stability of perovskite solar cells – A review. *Renew. Sustain. Energy Rev.* **77**, 131–146 (2017). doi: 10.1016/j.rser.2017.04.003
11. J. Huang, S. Tan, P. Lund, H. Zhou, Impact of H_2O on organic-inorganic hybrid perovskite solar cells. *Energy Environ. Sci.* **10**, 2284–2311 (2017). doi: 10.1039/C7EE01674C
12. P. Wang *et al*., Solution-Processable Perovskite Solar Cells toward Commercialization—Progress and Challenges. *Adv. Funct. Mater.* **29**, 1807661 (2019). doi: 10.1002/adfm.201807661
13. A. Dualeh *et al*., Effect of annealing temperature on film morphology of organic-inorganic hybrid pervoskite solid-state solar cells. *Adv. Funct. Mater.* **24**, 3250–3258 (2014). doi: 10.1002/adfm.201304022
14. B. Conings *et al*., Intrinsic Thermal Instability of Methylammonium Lead Trihalide Perovskite. *Adv. Energy Mater.* **5**, 1500477 (2015). doi: 10.1002/aenm.201500477
15. B. Philippe *et al*., Chemical and Electronic Structure Characterization of Lead Halide Perovskites and Stability Behavior under Different Exposures - a Photoelectron Spectroscopy Investigation. *Chem. Mater.* **27**, 1720–1731 (2015). doi: 10.1021/acs.chemmater.5b00348
16. N. K. Kim *et al*., Investigation of Thermally Induced Degradation in $CH_3NH_3PbI_3$ Perovskite Solar Cells using In-situ Synchrotron Radiation Analysis. *Sci. Rep.* **7**, 4645 (2017). doi: 10.1038/s41598-017-04690-w; pmid: 28680138
17. C. C. Boyd, R. Cheacharoen, T. Leijtens, M. D. McGehee, Understanding Degradation Mechanisms and Improving Stability of Perovskite Photovoltaics. *Chem. Rev.* **119**, 3418–3451 (2019). doi: 10.1021/acs.chemrev.8b00336; pmid: 30444609
18. T. Leijtens *et al*., Overcoming ultraviolet light instability of sensitized TiO_2 with meso-superstructured organometal tri-halide perovskite solar cells. *Nat. Commun.* **4**, 2885 (2013). doi: 10.1038/ncomms3885; pmid: 24301460
19. S. Ito, S. Tanaka, K. Manabe, H. Nishino, Effects of Surface Blocking Layer of Sb_2S_3 on Nanocrystalline TiO_2 for $CH_3NH_3PbI_3$ Perovskite Solar Cells. *J. Phys. Chem. C* **118**, 16995 (2014). doi: 10.1021/jp500449z
20. J. Ahmad, K. Bazaka, L. J. Anderson, R. D. White, M. V. Jacob, Materials and methods for encapsulation of OPV: A review. *Renew. Sustain. Energy Rev.* **27**, 104–117 (2013). doi: 10.1016/j.rser.2013.06.027
21. D. Yu, Y. Q. Yang, Z. Chen, Y. Tao, Y. F. Liu, Recent progress on thin-film encapsulation technologies for organic electronic devices. *Opt. Commun.* **362**, 43–49 (2016). doi: 10.1016/j.optcom.2015.08.021
22. A. Uddin, M. Upama, H. Yi, L. Duan, Encapsulation of Organic and Perovskite Solar Cells: A Review. *Coatings* **9**, 65 (2019). doi: 10.3390/coatings9020065
23. M. D. Kempe, A. A. Dameron, M. O. Reese, Evaluation of moisture ingress from the perimeter of photovoltaic modules. *Prog. Photovolt. Res. Appl.* **22**, 1159–1171 (2014). doi: 10.1002/pip.2374
24. F. J. Pern, R. Noufi, paper presented at SPIE Optics + Photonics, San Diego, CA, 16 October 2012.
25. L. Shi *et al*., Accelerated Lifetime Testing of Organic-Inorganic Perovskite Solar Cells Encapsulated by Polyisobutylene. *ACS Appl. Mater. Interfaces* **9**, 25073–25081 (2017). doi: 10.1021/acsami.7b07625; pmid: 28700216

26. F. Matteocci *et al*., Encapsulation for long-term stability enhancement of perovskite solar cells. *Nano Energy* **30**, 162–172 (2016). doi: 10.1016/j.nanoen.2016.09.041
27. Y. Han *et al*., Degradation observations of encapsulated planar $CH_3NH_3PbI_3$ perovskite solar cells at high temperatures and humidity. *J. Mater. Chem. A* **3**, 8139–8147 (2015). doi: 10.1039/C5TA00358J
28. H. C. Weerasinghe *et al*., New barrier encapsulation and lifetime assessment of printed organic photovoltaic modules. *Sol. Energy Mater. Sol. Cells* **155**, 108–116 (2016). doi: 10.1016/j.solmat.2016.04.051
29. Q. Dong *et al*., Encapsulation of Perovskite Solar Cells for High Humidity Conditions. *ChemSusChem* **9**, 2597–2603 (2016). doi: 10.1002/cssc.201601090; pmid: 27504719
30. J. Kim *et al*., An effective method of predicting perovskite solar cell lifetime–Case study on planar $CH_3NH_3PbI_3$ and $HC(NH_2)_2PbI_3$ perovskite solar cells and hole transfer materials of spiro-OMeTAD and PTAA. *Sol. Energy Mater. Sol. Cells* **162**, 41–46 (2017). doi: 10.1016/j.solmat.2016.12.043
31. G. E. Eperon *et al*., Formamidinium lead trihalide: A broadly tunable perovskite for efficient planar heterojunction solar cells. *Energy Environ. Sci.* **7**, 982 (2014). doi: 10.1039/c3ee43822h
32. W. Tan, A. R. Bowring, A. C. Meng, M. D. McGehee, P. C. McIntyre, Thermal Stability of Mixed Cation Metal Halide Perovskites in Air. *ACS Appl. Mater. Interfaces* **10**, 5485–5491 (2018). doi: 10.1021/acsami.7b15263; pmid: 29328620
33. C. Yi *et al*., Entropic stabilization of mixed A-cation ABX_3 metal halide perovskites for high performance perovskite solar cells. *Energy Environ. Sci.* **9**, 656–662 (2016). doi: 10.1039/C5EE03255E
34. M. Saliba *et al*., Incorporation of rubidium cations into perovskite solar cells improves photovoltaic performance. *Science* **354**, 206–209 (2016). doi: 10.1126/science.aah5557; pmid: 27708053
35. G. Grancini *et al*., One-Year stable perovskite solar cells by 2D/3D interface engineering. *Nat. Commun.* **8**, 15684 (2017). doi: 10.1038/ncomms15684; pmid: 28569749
36. N. Li *et al*., Mixed Cation $FA_xPEA_{1-x}PbI_3$ with Enhanced Phase and Ambient Stability toward High-Performance Perovskite Solar Cells. *Adv. Energy Mater.* **7**, 1601307 (2017). doi: 10.1002/aenm.201601307
37. Z. Wang *et al*., Efficient ambient-air-stable solar cells with 2D-3D heterostructured butylammonium-caesium-formamidinium lead halide perovskites. *Nat. Energy* **2**, 17135 (2017). doi: 10.1038/nenergy.2017.135
38. H. Tsai *et al*., High-efficiency two-dimensional Ruddlesden-Popper perovskite solar cells. *Nature* **536**, 312–316 (2016). doi: 10.1038/nature18306; pmid: 27383783
39. A. R. bin M. Yusoff, M. K. Nazeeruddin, Low-Dimensional Perovskites: From Synthesis to Stability in Perovskite Solar Cells. *Adv. Energy Mater.* **8**, 1702073 (2018). doi: 10.1002/aenm.201702073
40. Y. C. Kim *et al*., Engineering interface structures between lead halide perovskite and copper phthalocyanine for efficient and stable perovskite solar cells. *Energy Environ. Sci.* **10**, 2109–2116 (2017). doi: 10.1039/C7EE01931A
41. Y. Chen *et al*., Design of an Inorganic Mesoporous Hole-Transporting Layer for Highly Efficient and Stable Inverted Perovskite Solar Cells. *Adv. Mater.* **30**, 1805660 (2018). doi: 10.1002/adma.201805660
42. N. Arora *et al*., Perovskite solar cells with CuSCN hole extraction layers yield stabilized efficiencies greater than 20. *Science* **358**, 768–771 (2017). doi: 10.1126/science.aam5655; pmid: 28971968
43. E. Bi *et al*., Diffusion engineering of ions and charge carriers for stable efficient perovskite solar cells. *Nat. Commun.* **8**, 15330 (2017). doi: 10.1038/ncomms15330; pmid: 28604673
44. H. Tan *et al*., Efficient and stable solution-processed planar perovskite solar cells via contact passivation. *Science* **355**, 722–726 (2017). doi: 10.1126/science.aai9081; pmid: 28154242
45. M. Saliba *et al*., Cesium-containing triple cation perovskite solar cells: Improved stability, reproducibility and high efficiency. *Energy Environ. Sci.* **9**, 1989–1997 (2016). doi: 10.1039/C5EE03874J; pmid: 27478500
46. K. A. Bush *et al*., 23.6%-efficient monolithic perovskite/silicon tandem solar cells with improved stability. *Nat. Energy* **2**, 17009 (2017). doi: 10.1038/nenergy.2017.9
47. S. Seo, S. Jeong, C. Bae, N. G. Park, H. Shin, Perovskite Solar Cells with Inorganic Electron- and Hole-Transport Layers Exhibiting Long-Term (≈500 h) Stability at 85°C under Continuous 1 Sun Illumination in Ambient Air. *Adv. Mater.* **30**, e1801010 (2018). doi: 10.1002/adma.201801010; pmid: 29786887
48. K. A. Bush *et al*., Thermal and Environmental Stability of Semi-Transparent Perovskite Solar Cells for Tandems Enabled by a Solution-Processed Nanoparticle Buffer Layer and Sputtered ITO Electrode. *Adv. Mater.* **28**, 3937–3943 (2016). doi: 10.1002/adma.201505279; pmid: 26880196
49. C. C. Boyd *et al*., Barrier Design to Prevent Metal-Induced Degradation and Improve Thermal Stability in Perovskite Solar Cells. *ACS Energy Lett.* **3**, 1772–1778 (2018). doi: 10.1021/acsenergylett.8b00926
50. Y. I. Lee *et al*., A Low-Temperature Thin-Film Encapsulation for Enhanced Stability of a Highly Efficient Perovskite Solar Cell. *Adv. Energy Mater.* **8**, 1701928 (2018). doi: 10.1002/aenm.201701928
51. K. O. Brinkmann *et al*., Suppressed decomposition of organometal halide perovskites by impermeable electron-extraction layers in inverted solar cells. *Nat. Commun.* **8**, 13938 (2017). doi: 10.1038/ncomms13938; pmid: 28067308
52. R. Cheacharoen *et al*., Encapsulating perovskite solar cells to withstand damp heat and thermal cycling. *Sustain. Energy Fuels* **2**, 2398–2406 (2018). doi: 10.1039/C8SE00250A
53. Z. Li *et al*., Stabilizing Perovskite Structures by Tuning Tolerance Factor: Formation of Formamidinium and Cesium Lead Iodide Solid-State Alloys. *Chem. Mater.* **28**, 284–292 (2016). doi: 10.1021/acs.chemmater.5b04107
54. A. Dualeh, P. Gao, S. I. Seok, M. K. Nazeeruddin, M. Gratzel, Thermal Behavior of Methylammonium Lead-trihalide Perovskite Photovoltaic Light Harvesters. *Chem. Mater.* **26**, 6160–6164 (2014). doi: 10.1021/cm502468k
55. D. P. Nenon *et al*., Structural and chemical evolution of methylammonium lead halide perovskites during thermal processing from solution. *Energy Environ. Sci.* **9**, 2072–2082 (2016). doi: 10.1039/C6EE01047D
56. A. E. Williams *et al*., Perovskite processing for photovoltaics: A spectro-thermal evaluation. *J. Mater. Chem. A* **2**, 19338–19346 (2014). doi: 10.1039/C4TA04725G
57. L. Ma *et al*., Temperature-dependent thermal decomposition pathway of organic-inorganic halide perovskite materials. *Chem. Mater.* **31**, 8515–8522 (2019). doi: 10.1021/acs.chemmater.9b03190
58. E. J. Juarez-Perez, Z. Hawash, S. R. Raga, L. K. Ono, Y. Qi, Thermal degradation of $CH_3NH_3PbI_3$ perovskite into NH_3 and CH_3I gases observed by coupled thermogravimetry-mass spectrometry analysis. *Energy Environ. Sci.* **9**, 3406–3410 (2016). doi: 10.1039/C6EE02016J
59. E. J. Juarez-Perez *et al*., Photodecomposition and thermal decomposition in methylammonium halide lead perovskites and inferred design principles to increase photovoltaic device stability. *J. Mater. Chem. A* **6**, 9604–9612 (2018). doi: 10.1039/C8TA03501F
60. Z. Fan *et al*., Layer-by-Layer Degradation of Methylammonium Lead Tri-iodide Perovskite Microplates. *Joule* **1**, 548–562 (2017). doi: 10.1016/j.joule.2017.08.005
61. E. J. Juarez-Perez, L. K. Ono, I. Uriarte, E. J. Cocinero, Y. Qi, Degradation Mechanism and Relative Stability of Methylammonium Halide Based Perovskites Analyzed on the Basis of Acid-Base Theory. *ACS Appl. Mater. Interfaces* **11**, 12586–12593 (2019). doi: 10.1021/acsami.9b02374; pmid: 30848116
62. International Electrotechnical Commission, *Terrestrial photovoltaic (PV) modules - Design qualification and type approval - Part 1: Test requirements*; https://webstore.iec.ch/publication/24312.
63. A. Latini, G. Gigli, A. Ciccioli, A study on the nature of the thermal decomposition of methylammonium lead iodide perovskite, $CH_3NH_3PbI_3$: An attempt to rationalise contradictory experimental results. *Sustain. Energy Fuels* **1**, 1351–1357 (2017). doi: 10.1039/C7SE00114B
64. E. J. Juarez-Perez, L. K. Ono, Y. Qi, Thermal degradation of formamidinium based lead halide perovskites into sym-triazine and hydrogen cyanide observed by coupled thermogravimetry - mass spectrometry analysis. *J. Mater. Chem. A* **7**, 16912–16919 (2019). doi: 10.1039/C9TA06058H
65. I. L. Ivanov *et al*., Thermodynamics of formation of hybrid perovskite-type methylammonium lead halides. *J. Chem. Thermodyn.* **116**, 253–258 (2018). doi: 10.1016/j.jct.2017.09.026
66. J. Speight, *Lange's Handbook of Chemistry* (McGraw-Hill, ed. 16, 2005); www.accessengineeringlibrary.com/content/book/9780071432207/toc-chapter/chapter1/section/section83.
67. NIST Chemistry WebBook; https://webbook.nist.gov/chemistry/.
68. H. Bipp, H. Kieczka, Formamides. In *Ullmann's Encyclopedia of Industrial Chemistry* (Wiley-VCH, ed. 7, 2011), vol. 16.
69. A. F. Akbulatov *et al*., Light or Heat: What Is Killing Lead Halide Perovskites under Solar Cell Operation Conditions? *J. Phys. Chem. Lett.* **11**, 333–339 (2020). doi: 10.1021/acs.jpclett.9b03308; pmid: 31838849
70. B. A. Turowec, E. R. Gillies, Synthesis, properties and degradation of polyisobutylene–polyester graft copolymers. *Polym. Int.* **66**, 42–51 (2017). doi: 10.1002/pi.5250
71. R. Cheacharoen *et al*., Design and understanding of encapsulated perovskite solar cells to withstand temperature cycling. *Energy Environ. Sci.* **11**, 144–150 (2018). doi: 10.1039/C7EE02564E
72. Gas Chromatography Problem Solving and Troubleshooting. *J. Chromatogr. Sci.* **37**, 313 (1999). doi: 10.1093/chromsci/37.8.313

ACKNOWLEDGMENTS

We thank X. Deng for assistance in photoluminescence measurement, J. Zheng for assistance in proofreading the manuscript and providing valuable suggestions, and N. Proschogo (University of Sydney) for assistance in evaluating initial GC-MS techniques. **Funding:** The Australian Centre for Advanced Photovoltaics (ACAP) encompasses the Australian-based activities of the Australia-U.S. Institute for Advanced Photovoltaics (AUSIAPV) and is supported by the Australian Government through the Australian Renewable Energy Agency (ARENA). L.S. also thanks ARENA for scholarship funding support. **Author contributions:** L.S. and A.W.Y.H.-B. conceived and designed all the experimental work. L.S., T.L.Y., M.Z., D.S.L., J.B., and J.K. fabricated samples (perovskite thin-films and devices). L.S. encapsulated the samples and performed measurements. M.Z. assisted in producing the figures. M.P.B. contributed to the GC-MS methodology and assisted the measurement. N.T. and D.R.M. contributed to initiating the GC-MS idea and commenced initial measurements. L.H. and T.W. contributed to the discussion of pressure-tight sealing and decomposition reactions. The manuscript was written by L.S., M.P.B., and A.W.Y.H.-B. All authors contributed to the discussion of the data, proofread of the manuscript. The overall project was supervised by M.A.G., S.H., and A.W.Y.H.-B. **Competing interests:** The authors declare no competing interests. **Data and materials availability:** All data are available in the main text or the supplementary materials.

SUPPLEMENTARY MATERIALS

science.sciencemag.org/content/368/6497/eaba2412/suppl/DC1
Materials and Methods
Figs. S1 to S17
Tables S1 to S7
References (*73*–*78*)

16 November 2019; accepted 8 May 2020
Published online 21 May 2020
10.1126/science.aba2412

Gas chromatography–mass spectrometry analyses of encapsulated stable perovskite solar cells

Lei Shi, Martin P. Bucknall, Trevor L. Young, Meng Zhang, Long Hu, Jueming Bing, Da Seul Lee, Jincheol Kim, Tom Wu, Noboru Takamure, David R. McKenzie, Shujuan Huang, Martin A. Green and Anita W. Y. Ho-Baillie

Science **368** (6497), eaba2412.
DOI: 10.1126/science.aba2412originally published online May 21, 2020

Perovskite decomposition in detail

Solar cells are subject to heating when operating in sunlight, and the organic components of hybrid perovskite solar cells, especially the commonly used methylammonium cation, can undergo thermal decomposition. Encapsulation can limit decomposition by bringing such reactions to equilibrium and can prevent exposure to damaging ambient moisture. Shi *et al.* examined several encapsulation schemes for perovskite films and devices by probing volatile products with gas chromatography–mass spectrometry (see the Perspective by Juarez-Perez and Haro). Pressure-tight polymer/glass stack encapsulation was effective in suppressing gas transfer and allowed solar cells containing methylammonium to pass harsh moisture and thermal cycling tests.

Science, this issue p. eaba2412; see also p. 1309